Int. J. Electrochem. Sci., 17 **(2022)** Article Number: 220343, doi: 10.20964/2022.03.27

International Journal of
ELECTROCHEMICAL
SCIENCE
www.electrochemsci.org

Electrochemical and Theoretical Studies of Corrosion Inhibition Effect of *Durio zibethinus* Peel Extract on Copper in the Artificial Seawater

Yuxin Liu[1], *Yuzhe Hu*[1], *Hua Hao*[2,*], *Xingwen Zheng*[3]

[1] College of Chemistry and Materials Engineering, Beijing Technology and Business University, Beijing 100048, China;
[2] Institute of Chemistry, Chinese Academy of Sciences, Beijing 100190, China;
[3] Key Laboratory of Material Corrosion and Protection of Sichuan Province, Sichuan University of Science & Engineering, Zigong 643000, China
[*]E-mail: haohuaiccas@126.com

Received: 2 December 2021 / *Accepted:* 10 January 2022 / *Published:* 2 February 2022

The anticorrosion-active compounds were obtained from *Durio zibethinus* peel by ethanolic extraction (DZPE), which was experimentally and theoretically evaluated as an efficient corrosion inhibitor for copper in the artificial seawater (ASW). The inhibitory power of DZPE was confirmed by electrochemical and surface analyses. As indicated by potentiodynamic polarization tests, DZPE simultaneously suppressed anodic and cathodic reactions of copper in ASW, and thus yielded the reduced corrosion current density. Results of electrochemical impedance spectroscopy revealed that the charge transfer impedance at copper/solution interface was enhanced in the presence and with the augment of DZPE in ASW along with the improved surface passivation. By virtue of the interfacial adsorption, a well-protected morphology was observed for the copper after immersion in ASW with the optimum dosage of DZPE; and the adsorption of DZPE on copper surface conformed to Langmuir isotherm. Due to the favorable anticorrosion efficacy of DZPE, A largely restrained increase in surface roughness was acquired for the protected specimen as compared to the blank control. Reactive descriptors of the main components in DZPE with divergent chemical states were acquired via first-principles calculations under the dominant solvent model, which implied their potential interacting centers toward copper surface. The adsorption mechanism of each component in DZPE on Cu (110) plane was also revealed by molecular dynamics simulations.

Keywords: *Durio zibethinus* peel; plant extract; green corrosion inhibitor; density functional theory; molecular dynamics simulation

1. INTRODUCTION

Copper and its alloys are widely employed in numerous industrial sectors owing to their salient advantages such as excellent mechanical ductility, high thermal and electronic conductivity and relative

stability in the arid climate [1-3]. However, copper still suffers serious corrosion in aqueous solutions, especially those containing dissolved oxygen and/or chlorine ions, which has long been a widespread issue bothering both academic and industrial communities [4]. For example, copper-based facilities are severely corroded in marine environment due to the heavy causticity of seawater [5]. Even worse, corrosion of copper may silently deteriorate the structural equipment to an irretrievable degree, lower the production efficiency, and ultimately threaten the safety of human and eco-system [6-8]. Therefore, tremendous endeavors have been devoted to solving the burden posed by metal corrosion.

Typically, using corrosion inhibitors is a cost-effective and high-efficient alternate to mitigate metal degradation [9-11]. Organic corrosion inhibitors with heteroatoms (e.g. N, S and O), multiple bonds and/or π-conjugated system can adsorb on metal surface via the electron-orbital binding, which surpass some hazardous inorganic counterparts such as nitrite and chromate [12, 13]. Nonetheless, plenty of organic inhibitors still arouse controversy on the demand of biodegradability and environmental tolerance. In recent year, seeking solutions from natural plants is deemed as a sustainable strategy to establish the environmentally friendly protocol for retarding metal dissolution in the aggressive media [14-16]. Hence, the renewable, handily available and biodegradable plant extracts have been increasingly studied and practically applied for metal protection. For instance, Farhadian and co-workers [17] employed modified sunflower oil as a sustainable inhibitor, which exerted favorable anticorrosion effect for mild steel in 15% HCl medium with a maximum efficiency of 93% even at 353 K. Zhang et al. [18] extracted the inhibitor (IFE) from *Idesia polycarpa* Maxim fruits for copper in 0.5 M H_2SO_4 solution; electrochemical and surface analyses indicated that IFE effectively retarded copper corrosion by the outstanding interfacial adsorption.

In addition to experimental research, theoretical modelling was frequently deployed to better understand the anticorrosive mechanism of inhibitors for metals in various media. Typically, Obot et al. [19] explicitly pointed out that efficient anticorrosion chemicals could be designed with the aid of density functional theory (DFT), in which reactive descriptors of inhibitors had a close correlation with the protective efficiency for metals in corrosive solutions. Verma et al. [20] summarized advances in the utilization of molecular dynamics (MD) and Monte Carlo simulations for exploring the adsorption nature of inhibitors at metal/solution interface, which turned out to be powerful tools to probe the underlying anticorrosion mechanism.

In this work, the biomass waste, *Durio zibethinus* peel, was selected as the raw material for extracting corrosion inhibitor (DZPE) for copper in the artificial seawater (ASW). The special fragrance of this fruit waste inspired us to evaluate its protection efficacy for copper, which originates from N, S-containing compounds. Potentiodynamic polarization and electrochemical frequency modulation (EFM) techniques were performed to clarify the kinetic properties of uninhibited and inhibited copper specimens in ASW. Besides, the relevant impedance characteristics of the specimens were disclosed by electrochemical impedance spectroscopy (EIS). The inhibitory effect of DZPE was clearly examined by multidimensional surface analyses for the immersed copper. Theoretical simulations were conducted to deeply disclose the anticorrosive mechanism of DZPE. To our best knowledge, the elucidation of inhibitive mechanism of DZPE by both experimental and theoretical approaches for copper in ASW has not been reported; and this study may provide valuable guidance for the choice of plant extract and the interpretation of mechanism toward copper protection in marine environment.

2. EXPERIMENTAL SECTION

2.1 Raw Materials

All chemicals mentioned herein were of analytical pure and used as received. Anhydrous ethanol, NaCl, $MgCl_2$, Na_2SO_4, $CaCl_2$, KCl, $NaHCO_3$, KBr, H_3BO_3, $SrCl_2$ and NaF were commercially acquired from Beijing Bio-Chem Company (China). An EDIA-100-UP ultrapure system provided deionized water for the solution preparation. *Durio zibethinus* peel was collected from the fructus imported from Thailand in June, 2021. Standard copper specimens with a dimension of 50 mm × 25 mm × 2 mm were purchased from Tianjin Aida Co., Ltd. and utilized as the metal substrate. As per the convention in ASTM D1141, ASW was prepared following the protocol listed in Table 1.

Table 1. The formula of ASW as regulated in ASTM D1141

Chemical	NaCl	$MgCl_2$	Na_2SO_4	$CaCl_2$	KCl	$NaHCO_3$	KBr	H_3BO_3	$SrCl_2$	NaF
Concentration (g/L)	24.5	5.2	4.1	1.2	0.7	0.2	0.1	0.03	0.03	0.003

2.2 Extraction, isolation and characterization of DZPE

The naturally dried *Durio zibethinus* peel (100 g) was crushed and macerated in ethanol/water (0.75/0.25, volume) mixture at 323 ± 0.5 K for five days. Then, the mixture was transferred to a rotary evaporator under reduced pressure at 343 K to remove the volatile ingredients. Afterwards, the crude extract was centrifuged at 4500 r/min; subsequently, the supernatant was collected, vacuum-dried at 328 K overnight, and ultimately the faint yellow solids (yield: 30.25%) were obtained and labeled as DZPE. Phytochemical screening of DZPE was performed from both reported literatures and our experimental verifications [21-23], and the desired analytes are summarized in Scheme 1. The functional groups in DZPE was confirmed by a Nicolet iN10 MX Fourier transform infrared spectroscopy (FTIR, Thermo Scientific, USA) by KBr flake in the wavenumber from 4000 to 400 cm^{-1}. Also, X-ray diffraction pattern of DZPE was recorded with a 2θ of 5°-80° (step size: 0.1°) by an X'Pert powder diffractometer (XRD, Panalytical, the Netherlands) employing Cu Kα as the excitation source to ascertain the phase state of DZPE.

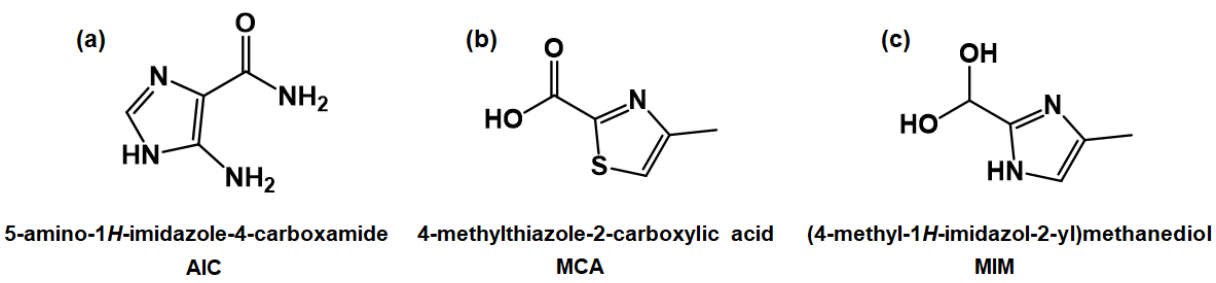

5-amino-1*H*-imidazole-4-carboxamide
AIC

4-methylthiazole-2-carboxylic acid
MCA

(4-methyl-1*H*-imidazol-2-yl)methanediol
MIM

Scheme 1. Anticorrosion-active phytochemical components of *Durio zibethinus* peel extract: (a) AIC, (b) MCA and (c) MIM

2.3 Electrochemical measurements

Copper specimens were degreased in anhydrous ethanol, and successively abraded with the emery paper ranging from 200 to 2000 grit, and followed by the polishing on a piece of artificial schammy. The elaborated specimens were flushed alternately by running deionized water and ethanol, ultrasonically cleaned to remove debris and mounted on a flat test cell leaving an effective area of 1 cm^2 (250 mL, Gaoss-Union, Wuhan, China) to accomplish electrochemical measurements. Therein, copper, $Ag/AgCl_{sat}$ and platinum sheet (1 cm^2) were assembled as the working, reference and auxiliary electrodes, respectively. All electrochemical determinations were fulfilled via an Autolab PGSTAT302N workstation (Metrohm, Switzerland) at 298 ± 1.5 K.

A stable open circuit potential (E_{ocp}) was preferentially conditioned for working electrode after 30 min exposure in ASW at 298 K. Then, potentiodynamic polarization and EIS tests were respectively conducted for copper in the uninhibited and inhibited solutions by DZPE. In detail, polarization curve was scanned in a potential from -250 to 250 mV (*vs*. E_{ocp}) with a sweep rate of 1 mV/s. EIS was performed under E_{ocp} with a frequency band between 10^5 and 10^{-2} Hz using a sinusoidal amplitude of 10 mV. Coupling the established impedance characteristics with actual breakpoint frequency, EFM spectra were recorded at a base frequency of 0.1 Hz using 2 and 5 as multiplicities; and 32 cycles of sinusoidal waveform were applied with an amplitude of 10 mV. Each electrochemical assay ran in triplicate to ensure the reproducibility. The in-built Nova 2.1 code was utilized to resolve the relevant data, in which the quantity mean values were reported with acceptable standard deviation.

2.4 Surface examinations

A QUANTA FEG 250 scanning electron microscope (SEM, FEI, USA) was employed to capture the surface morphologies of different copper specimens. Atomic force microscopy (AFM, FastScan, Bruker, Germany) was exploited under tapping mode to obtain the topographies of specimens in nano-/micro-scale. Interfacial wettability was gauged through an OCA35 contact angle meter (Dataphysics, Germany) at 298 K by sessile drop method. The adsorption layer on copper surface after 72 h exposure in ASW with the optimum dosage of DZPE was confirmed by attenuated total reflection FTIR (ATR-FTIR) in a wavenumber from 4000 to 500 cm^{-1} through the same instrument stated in Section 2.2.

2.5 Theoretical simulations

Theoretical simulations were completed using Materials Studio suite (BIOVIA Inc., France). First-principles DFT calculations were fulfilled through DMol3 package. Initially, the macro-species of target compounds were analyzed by Marvin-Sketch software to ascertain their accurate chemical states. Based on multiscale simulations, dominant solvent models for AIC, MCA and MIM were constructed to involve the ion-dipole interaction during DFT calculations. Each model was fully optimized in the given symmetry using GGA treated by PBE exchange-correlation. All-electron double-numerical atomic orbital augmented by d-polarization (DNP) was deployed as the basis set.

MD simulations was realized via Forcite plus module under self-built InterfaceFF forcefield to better describe the chemical interaction at copper/solution interface [5, 15]. Owing to the highest surface energy, Cu (110) plane was chosen as the surface for the adsorption of inhibitor. Five layers of this plane was cleaved (frozen before simulation), and a vacuum layer of 20 Å thickness was built over the topmost copper atoms to avoid Coulomb interference from other periodic images. A 6 × 8 supercell was enlarged to form a simulation box with a dimension of 29.2 Å × 31.5 Å × 35.7 Å. For the simplification of experimentally used corrosive solution, 350 water molecules (1 g/cm^3), 5 Na^+, 5Cl^- and one inhibitor were involved in the box to perform the dynamic relaxation with large scale timespan of 1000 ps (step: 1 fs) under *NVT* (constant atom numbers, system volume and temperature) ensemble at 298 K kept by Nose thermoset.

3. RESULTS AND DISCUSSION

3.1 Characterization of DZPE

To ascertain the active functional groups, FTIR and XRD examinations were performed on DZPE. Figure 1a displays the FTIR spectrum of DZPE. The broad band centered at 3345 cm^{-1} is assigned to the stretching of -OH and/or -NH_2 [24]. The peak at 2898 cm^{-1} is identified as the stretching vibration of methyl and/or methylene [5].

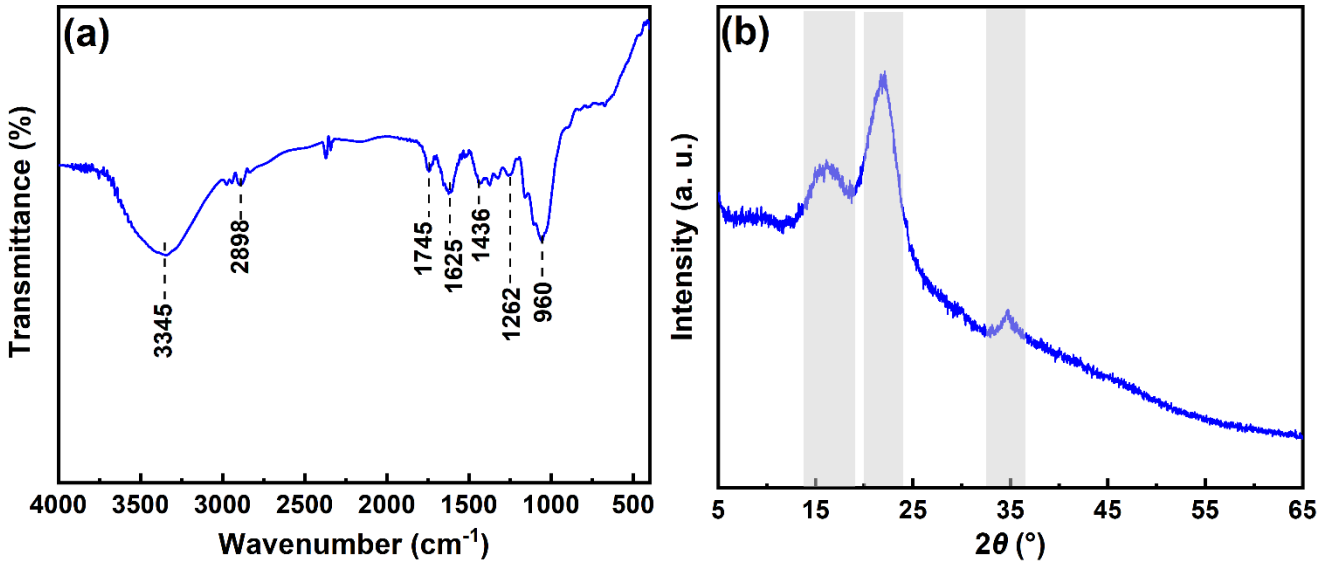

Figure 1. FTIR spectrum (a) and XRD pattern (b) of *Durio zibethinus* peel extract

The stretching of C-S on thiazole ring is found at the band of 1745 cm^{-1}; while, the peak at 1625 cm^{-1} corresponds to the stretching of C=O on amide group [22, 25]. A series of peaks between 1436 and 1262 cm^{-1} associated with backbone vibration of imidazole ring with the corresponding C-H vibration peak at 960 cm^{-1} [26]. The analysis of FTIR agrees well with the screened compounds given in Scheme

1, which also indicate their content-predominance in DZPE. In addition, XRD pattern of DZPE in Figure 1b shows that broad diffraction peaks at 16.05° (d = 0.55 nm), 21.83° (d = 0.41 nm) and 34.67° (d = 0.26 nm), revealing the inferior crystalline. Notably, some characteristic diffractions related to the insoluble essential oil in *Durio zibethinus* peel are scarcely found in the XRD pattern, which may result from the degreasing procedure in the preparing procedure [21]. The inferior crystalline and lack of insoluble substances suggest the favorable solubility of DZPE in the aqueous solution, and prompt the ensuing anticorrosion effect for metals by virtue of heteroatoms (e.g., O, N and S) on the constituents.

3.2 Electrochemical analysis

3.2.1 Electrochemical kinetics

The inhibitory kinetics of DZPE for copper in ASW was evaluated by potentiodynamic polarization. Initially, E_{ocp} was recorded with the augment of time for copper in ASW with various DZPE concentration at 298 K; and the results are illustrated in Figure 2a. Obviously, all plots tend to be equilibrium after 30 min immersion, disclosing a pseudo-stable state of copper surface in ASW. It is highlighted that final E_{ocp} value of each DZPE-inhibited specimen is nobler than that associated with blank control. This demonstrates the favorable corrosion mitigation ability of DZPE from the thermodynamic view [4]. Figure 2b presents polarization curves for copper in ASW without and with various dosages of DZPE at 298 K. As is seen, both cathodic and anodic curves shift to the low-current density region upon the addition of DZPE, implying that cathodic reduction and anodic dissolution are simultaneously retarded in the presence of the extract [27]. Moreover, the synchronous suppression of anodic and cathodic curves infers that DZPE acts as a mix-type inhibitor for copper in the brine [28]. Also worthy of note in Figure 2b, the suppress effect for anodic and cathodic branches is concentration-dependent, which is enhanced with the increase in DZPE dosage. This suggests that the anticorrosive capacity of DZPE is assigned to the effective adsorption of specific components on copper surface. Higher concentration of the inhibitor inevitably yields the larger coverage on metal surface, and hence exerts better inhibition capability for the charge exchange at metal/solution interface [29].

Linear extrapolation of polarization plots was executed to obtain electrochemical kinetic parameters such as corrosion current density (i_{corr}), corrosion potential (E_{corr}), anodic (β_a) and cathodic (β_c) Tafel slopes, which are listed in Table 2. The protective efficiency (η_i) can be calculated from i_{corr} values [30]:

$$\eta_i = (i_{corr}^{blank} - i_{corr}^{inh})/i_{corr}^{blank} \times 100\% \quad (1)$$

where i_{corr}^{blank} and i_{corr}^{inh} are the current densities of copper specimens in the blank and DZPE-containing ASW, respectively. It is clear in Table 2 that E_{corr} has a noble movement as the concentration of DZPE augments with a maximum shift of 29 mV (module value, less than 85 mV). This means that DZPE can be regarded as the anodic-controlled mix-type corrosion inhibitor [31]. Besides, the insufficient shift of E_{corr} also implies the geometric shielding of corrosion-sensitive centers on copper surface by DZPE components to impede the substrate dissolution [12, 32]. The value of i_{corr} gradually decreases with the increase in DZPE concentration, and reaches 0.93 μA/cm^2 at 0.7 g/L harvesting a η_i value of 95.28%. The decrease in i_{corr} should stem from the adsorption of DZPE on copper surface, and

the consequent formation of protective layer isolating copper from corrosive ions in the bulk solution [2]. Feeble improvement of η_i (95.38%) is found after further elevating DZPE concentration to 0.9 g/L, indicating that the adsorption of active components becomes dynamic saturation [33]. Furthermore, the changes of β_a and β_c are indistinctive for each protected system except the specimen with 0.1 g/L DZPE, which reveal the almost unaffected corrosion mechanism of copper in ASW without and with the extract [16]. Once again, the relatively stable Tafel slopes evidence that the steric shielding due to DZPE adsorption plays a key role in inhibiting copper corrosion in ASW.

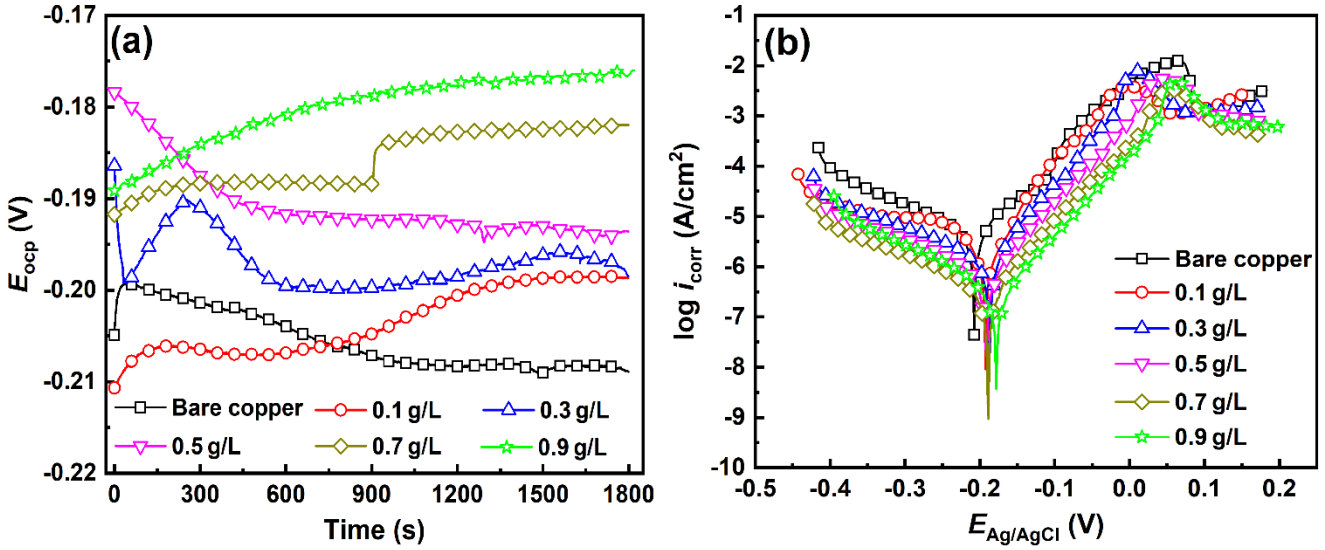

Figure 2. Plots of E_{ocp} *versus* time (a) and potentiodynamic polarization for copper in ASW without and with various concentrations of DZPE at 298 K

Table 2. Polarization parameters for copper in ASW without and with various DZPE concentrations at 298 K

C_{DZPE} (g/L)	E_{corr} (mV)	i_{corr} (μA/cm^2)	β_a (mV/dec)	-β_c (mV/dec)	η_i (%)
0	-208	19.71	93	117	/
0.1	-193	4.54	128	122	76.97
0.3	-191	2.30	95	120	88.33
0.5	-188	1.82	97	116	90.77
0.7	-187	0.93	99	121	95.28
0.9	-178	0.91	93	118	95.38

As an emerging and non-destructive electrochemical technique, EFM can rapidly acquire the kinetic indices for metal corrosion in aggressive solutions [34]. The EFM spectra for copper in ASW without and with various concentrations of DZPE at 298 K are summarized in Figure 3. For the spectra in Figure 3a, both harmonic and intermodulation responses at the respective frequencies are apparently more pronounced than background noises validating the effectiveness of measurements [35]. Moreover,

the spectrum is continuously suppressed with the augment of DZPE concentration, indicating the efficient anti-corrosion effect of the extract [36]. Another aspect, the peak current densities are comparable between the neighboring intermodulation frequencies such as 0.3 and 0.7 Hz, which earn the possibility to derive kinetic parameters including corrosion current density ($i_{\text{corr-F}}$), causality factors 2 (CF2) and 3 (CF3). In light of the passivation features of copper in brine media (verified by EIS, *vide infra*), the diffusion-controlled model was utilized to acquire the kinetic indices, in which the relevant parameter can be expressed by the following equations [37]:

$$i_{\text{corr-F}} = i_{\omega 1,\omega 2}^2 / 2i_{\omega 2 \pm \omega 1} \quad (2)$$

$$\text{CF2} = i_{\omega 2 \pm \omega 1} / i_{2\omega 1} \quad (3)$$

$$\text{CF3} = i_{2\omega 2 \pm \omega 1} / i_{3\omega 1} \quad (4)$$

where $i_{\omega 1,\omega 2}$ is the current density at the excited frequency, i.e. 0.2 and 0.5 Hz; $i_{\omega 2 \pm \omega 1}$ and $i_{2\omega 2 \pm \omega 1}$ are the current densities at the intermodulation frequencies of $\omega 2 \pm \omega 1$ and $2\omega 2 \pm \omega 1$, respectively; $i_{2\omega 1}$ and $i_{3\omega 1}$ are the current densities at harmonic frequencies, i.e. two and three times of base frequency, respectively. As per the derived $i_{\text{corr-F}}$ value, the inhibitory efficiency (η_{F}) can be calculated by the relationship [38]:

$$\eta_{\text{F}} = (i_{\text{corr-F}}^{\text{blank}} - i_{\text{corr-F}}^{\text{inh}}) / i_{\text{corr-F}}^{\text{blank}} \times 100\% \quad (5)$$

where $i_{\text{corr-F}}^{\text{blank}}$ and $i_{\text{corr-F}}^{\text{inh}}$ are the corrosion current densities of copper specimens in ASW without and with various concentrations of DZPE, respectively.

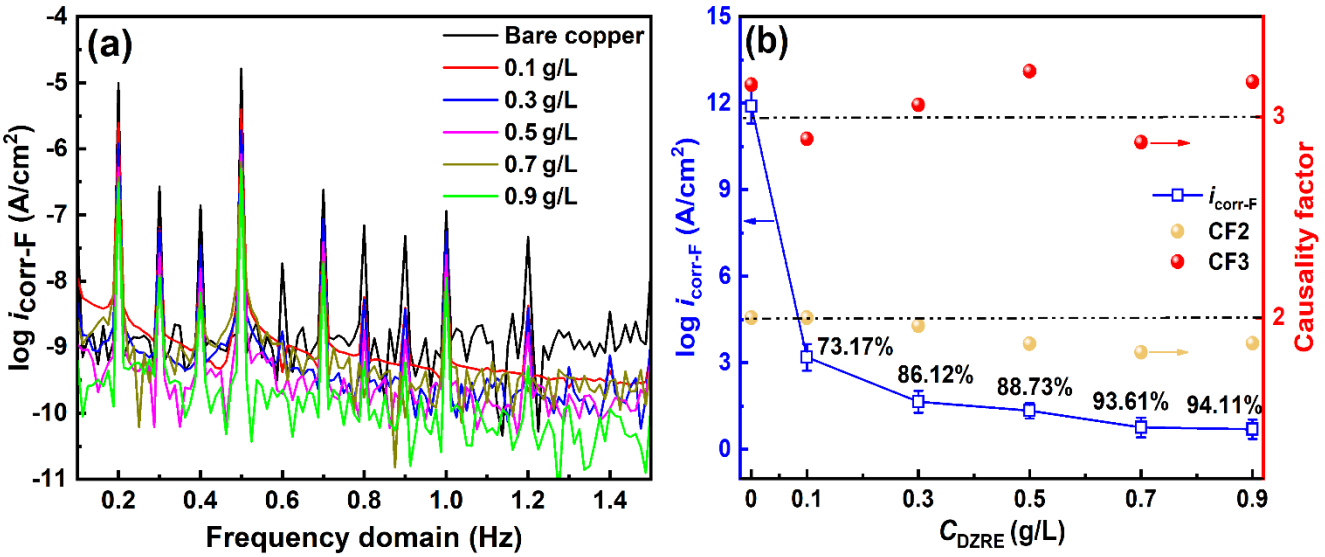

Figure 3. EFM spectra (a) and the corresponding kinetic parameters of copper in ASW without and with various concentrations of DZPE at 298 K (η_{i} values locate over the symbols of $i_{\text{corr-F}}$)

The kinetic parameters derived from EFM spectra are depicted in Figure 3b. Clearly, all CF2 and CF3 indexes close to the respective ideal values (i.e. 2 and 3) for each system, articulating the validation of EFM determinations. Similar as the polarization tests, $i_{\text{corr-F}}$ monotonously declines as the concentration of DZPE increases. Accordingly, η_{F} value gradually augments, and attains 94.11% with a DZPE dosage of 0.9 g /L. Noteworthily, η_{F} corresponded to the copper specimen with 0.9 g/L DZPE is

comparable with that associated with 0.7 g/L-inhibited system (93.61%). This reveals that the adsorption of DZPE on copper surface is inclined to be saturation at a dosage over 0.7 g/L. In summary, the kinetic features obtained from EFM measurements are in line with those reflected by polarization measurements.

3.2.2 EIS

EIS is the other non-destructive technique to probe the anticorrosive mechanism of inhibitors for metals in aggressive media [11]. Nyquist and Bode spectra for copper in ASW without and with various concentrations of DZPE at 298 K are displayed in Figure 4a and b, respectively. In Figure 4a, Nyquist diagrams for specimens protected by DZPE are memorably larger than the blank control (inset of Figure 4a). This is attributed to the effective corrosion inhibition of DZPE for copper in ASW due to interfacial adsorption [39]. The diameter of Nyquist loop is enlarging with the increasing DZPE concentration, which designates the elevated charge transfer resistance at the copper/solution interface. Besides, the intensified inhibitory strength by elevating DZPE dosage is also evidenced by Bode modulus plots given in Figure 4b, in which the low-frequency resistance at 0.01 Hz gradually ascends with the rise in DZPE dosage. The slope of linear segment at medium-frequency region approaches to the unity for each modulus curve, implying the pseudo-capacitive nature of copper/solution interface due to the passivated and inhibitor-adsorbed layer [32]. As DZPE concentration increases, the absolute value of Bode phase angle gets closing to 90° along with the broaden peak, which also benefits from the adsorption of inhibitor on copper surface. The inhibitor adsorption weakens the heterogeneity of copper surface, in turn, enhances the interfacial capacitive behavior, and thereby elevates the phase angle [40, 41]. Scrutiny of Figure 4b finds that double-time constant is confirmed for the electrochemical process of copper in ASW without and with various DZPE concentrations. Accordingly, equivalent circuits described in Figure 4c and d are proposed to in-depth explore the impedance features of copper/solution interface. In detail, the circuit model in Figure 4c is employed to fit EIS data with Warburg diffusion (*W*); while, the other one is suitable for the data without *W*. Constant phase-angle element (*Q*) was adopted in the fitting procedure to compensate the dispersion effect caused by surface heterogeneity of solid electrodes, whose impedance (Z_Q) can be calculated by the following expression [42]:

$$Z_Q = Y_0^{-1} \times (j\omega)^{-n} \quad (6)$$

where Y_0 is the constant of *Q*; *j* is the image root ($j^2 = -1$); ω is the angular frequency ($2\pi f$); and *n* is the phase shift index, exemplifying the smoothness scale of metal surface.

Subsequent to the fitting procedure, the impedance parameters, such as film resistance (R_f), charge transfer resistance (R_{ct}) and the impedance of *W*, were derived and are listed in Table 3. The inhibitory efficiency (η_z) can be acquired by the equation:

$$\eta_z = (R_{ct}^{inh} - R_{ct}^{blank})/R_{ct}^{inh} \times 100\% \quad (7)$$

where R_{ct}^{blank} and R_{ct}^{inh} are the charge transfer resistances for copper in ASW without and with various concentrations of DZPE, respectively. Considering the emerged capacitive features in Figure 4a and b, the capacitance of surface film (C_f) and double layer (C_{dl}) were calculated as per the expressions [27]:

$$C_f = Y_0 \times (\omega_{max})^{n-1} \quad (8)$$

$$C_{dl} = [Y_{dl} \times R_{ct}^{1-n}]^{1/n} \quad (9)$$

where ω_{max} is the maximum imaginary angular frequency; and Y_{dl} is the constant of Q_{dl}. As tabulated in Table 3, the resistances (R_f and R_{ct}) of copper surface are enhanced with the increase in DZPE concentration. Especially, R_{ct} significantly increases from 1.27 kΩ·cm^2 for bare copper to 18.25 kΩ·cm^2 with 0.9 g/L DZPE in ASW. On one hand, the presence of DZPE favors to reinforce the pre-formed passivation film over copper surface isolating the damage of corrosive ions in ASW, and thus elevates R_f value. On the other hand, the charge transfer between copper surface and bulk solution is effectively depressed owing to the formation of insulating barrier by DZPE adsorption [43].

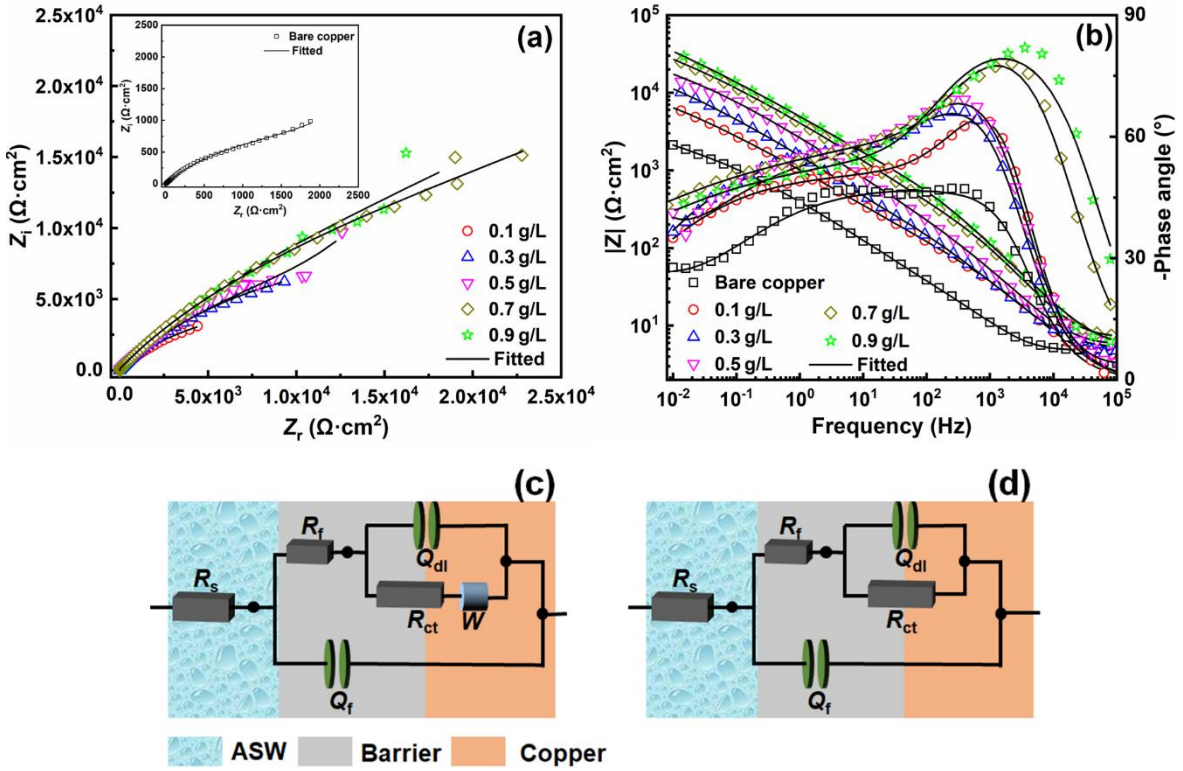

Figure 4. Nyquist (a) and Bode (b) plots of copper in ASW without (inset) and with different concentrations of DZPE at 298 K attached by the corresponding equivalent circuits (c and d)

Because of the improved R_{ct} value, the maximum η_z achieves as 93.04% at 0.9 g/L dosage of DZPE. On the contrary, the reduction of C_f and C_{dl} is found in Table 3 in the presence and with the augment of DZPE concentration. The semiconducting passivation film may be responsible for the diminishing C_f value [12]. Meanwhile, the decline of C_{dl} from 118.94 (bare copper) to 35.03 μF/cm^2 (protected by 0.9 g/L DZPE) is attributed to the adsorption of inhibitor as stated by Helmholtz model [37, 44]:

$$C_{dl} = (\varepsilon_0 \varepsilon_{0i}/h) \times A \quad (10)$$

where h is the thickness of double layer; A is the effective area of electrode surface; ε_0 and ε_{0i} are the respective dielectric constants of air and adsorbed layer. The substitution of water and/or ions by

DZPE adsorption on copper surface fatally increases *h* and dampens *in-situ* dielectric constant, and consequently attenuates C_{dl} value. Thanks to the improved interfacial homogeneity, n_f and n_{dl} gradually close to unity as DZPE concentration increases [45]. Furthermore, the uniform and homogeneous adsorption layer is prone to retard the diffusion of ions and corroded species at the copper/solution interface; therefore, *W* value is apparently decreased with the increase in DZPE concentration until the annihilation of diffusion phenomenon for the specimens with 0.7 and 0.9 g/L inhibitor in ASW. Ultimately, the comprehensive comparison of different electrochemical data indicates that the inference on inhibitory mechanism of DZPE for copper in ASW coincides well with each other.

Table 3. Impedance parameters of copper in ASW without and with different concentrations of DZPE at 298 K

C_{DZPE} (g/L)	R_f ($\Omega \cdot cm^2$)	C_f ($\mu F/cm^2$)	n_f	R_{ct} ($k\Omega \cdot cm^2$)	C_{dl} ($\mu F/cm^2$)	n_{dl}	W ($\Omega \cdot cm^2 \cdot s^{1/2}$)	η_z (%)
0	146.39	35.25	0.57	1.27	118.94	0.79	3.84×10^{-3}	/
0.1	187.37	31.74	0.59	5.02	89.30	0.81	1.17×10^{-3}	74.70
0.3	208.18	23.81	0.67	7.89	75.23	0.85	1.02×10^{-3}	83.90
0.5	225.46	20.11	0.66	11.92	55.81	0.89	6.62×10^{-4}	89.35
0.7	271.04	18.57	0.73	17.30	48.26	0.91	/	92.66
0.9	299.75	11.29	0.76	18.25	35.03	0.93	/	93.04

3.3 Surface analysis

Apart from electrochemical measurements, the inhibitory capacity of DZPE can be visually examined by multidimensional observations. Figure 5 summarizes the surface morphologies, topographies and interfacial wettability of copper before and after 72 h immersion in ASW with 0.9 g/L DZPE at 298 K. As depicted in Figure 5a, the freshly polished copper surface exhibits a flat and clean appearance giving a water contact angle of 48.1°, which is also supported by the 3D topography shown in Figure 5d. The average roughness for the polished specimen is measured as 114.29 nm that is mainly assigned to the mechanical scratches. For the specimen after 72 h immersion in blank ASW, corroded surface with dispersed pits and crevices is found in Figure 5b. The water contact angle is lowered to 24.6° induced by the capillary effect of surface defects [46]. Accordingly, Figure 5e presents a severely roughened and heterogeneous topography caused by the corrosive attack from dissolved ions (e.g. Cl^-) and/or oxygen, in which the roughness hugely increases to 720.75 nm. In contrast, the morphology in Figure 5c clearly indicates a well-protected appearance after immersion with the optimum DZPE concentration since the polished scratches can be still distinguished. A surface of approximately hydrophobic wettability is acquired earning a water contact angle of 88.9° for the adsorption of low-polarity constituents in DZPE, which prevents the underneath substrate from the attack of corrosive species. Owing to the protective DZPE-adsorbed layer, small amount of adherent corroded resultants and/or components in the extract are detected over copper surface (Figure 5f); and the average roughness slightly increases to 251.43 nm as compared to the polished counterpart.

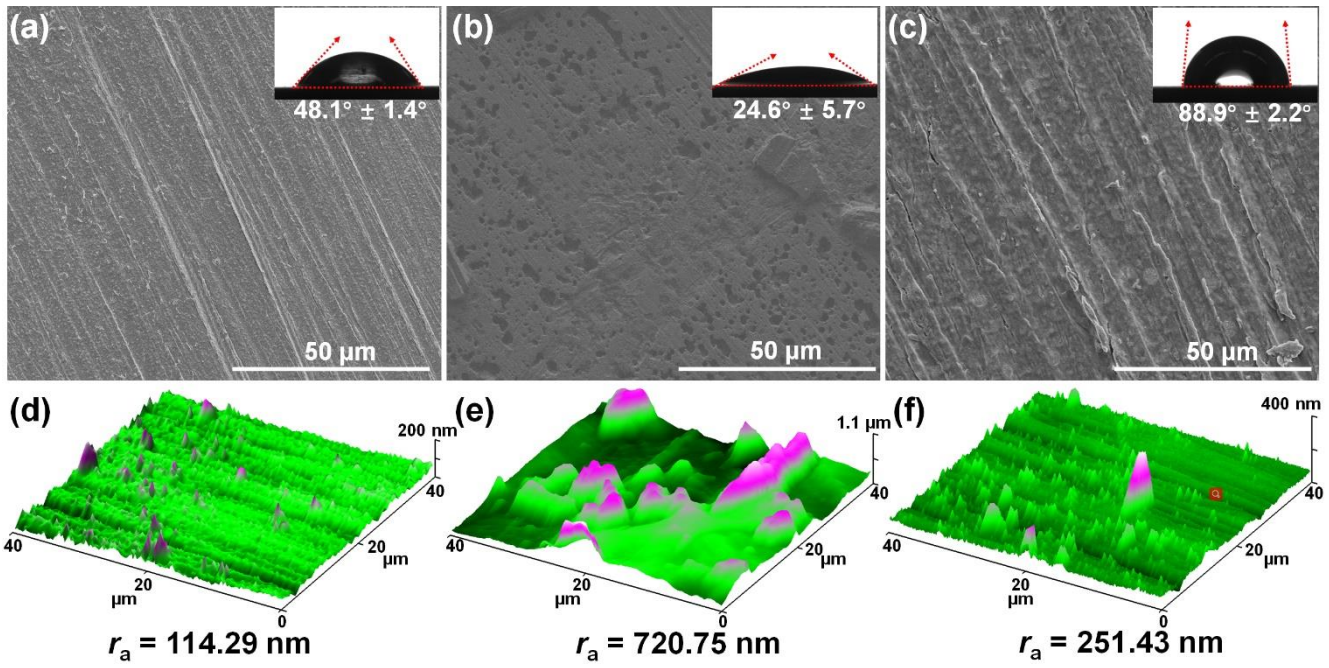

Figure 5. SEM images (inset: wettability; upper) and AFM topographies (lower) of freshly polished copper (a, d), corroded (b, e) specimen and the inhibited specimen (c, f) with 0.9 g/L DZPE after 72 h immersion in ASW at 298 K

The adsorption of DZPE on copper surface can be documented by ATR-FTIR spectrum shown in Figure 6a. As displayed, the peaks at 3507 and 3302 cm^{-1} are assigned to the stretching of -OH and -NH_2, respectively [4, 26]. The peak at 1750 cm^{-1} is identified as the stretching of C-S; while that at 1617 cm^{-1} associates with the stretching of C=O on amide group [25]. The adsorption bands ranging from 1433 to 1254 cm^{-1} can be attributed to the breathing of imidazole ring [24]. The aforementioned characteristic peaks collectively demonstrate the effective adsorption of proposed components (Scheme 1) on copper surface. Additional comparison between the spectra in Figure 6a and Figure 1a indicates that both hypochromic and bathochromic shifts emerge for the functional groups after interfacial adsorption. This convincingly consolidates that the adsorption of DZPE on copper comprises of both physical and chemical interaction between reactive groups and metal surface [7].

On that account, it is necessary to investigate the interaction nature between DZPE and copper surface, which can be realized by various adsorption isotherms [47]. The inhibitory efficiencies derived from polarization, EFM and EIS measurements were utilized to accomplish the isotherm fitting. Thereinto, Langmuir isotherm best describes the adsorption behavior of DZPE, which can be expressed as follows [15]:

$$\theta = \eta/100 \quad (11)$$

$$C_{DZPE}/\theta = 1/K_{ads} + C_{DZPE} \quad (12)$$

where θ is the surface coverage by adsorbed DZPE; η is the inhibitory efficiencys obtained from different electrochemical tests; C_{DZPE} is the concentration of DZPE in ASW; and K_{ads} is adsorption/desorption constant. The fitting lines are depicted in Figure 6b, in which the nearly ideal square deviations (R^2) disclose the feasibility of Langmuir model. In addition, all slopes of fitted lines

are in the exceedingly adjacent of unity, revealing the monolayer nature of DZPE film without lateral interaction among adsorbed species [44]. Adsorption thermodynamic features can be derived from the isotherm fitting as per the following equation:

$$\Delta G_{ads} = -RT \times \ln(1000 \times K_{ads}) \quad (13)$$

where ΔG_{ads} is standard Gibbs free energy of the adsorption process; R is gas contant; T is Kelvin temperature; and 1000 means the mass concentration of water in g/L. The calculated ΔG_{ads} values for fitting data from polarization, EFM and EIS tests are -30.48, -32.16 and -31.71 kJ/mol, respectively. Negative sign of ΔG_{ads} signifies the spontaneous adsorption of DZPE and the stability of ensuing protective layer on copper surface [13]. Notably, the magnitude of ΔG_{ads} lies between -20 and -40 kJ/mol, revealing that the adsorption of constituents in DZPE undergoes a physicochemical manner [28].

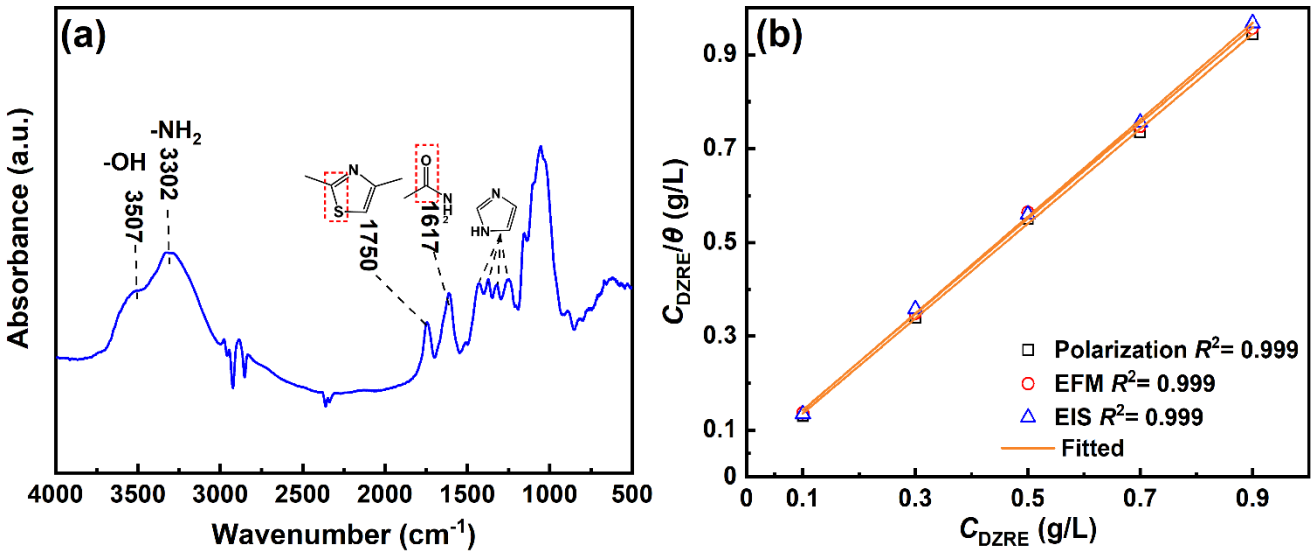

Figure 6. ATR-IR spectrum of copper surface after 72 h immersion in ASW with 0.9 g/L DZPE at 298 K (a) and Langmuir isotherm fitting for DZPE adsorption based on different electrochemical techniques

3.4 Theoretical simulation

3.4.1 DFT calculations

Electron-structural descriptors were obtained through DFT calculations to correlate the theoretical indices with experimental results. Macro-species analysis was preferentially performed on targeted compounds to clarify their detailed chemical states in ASW (pH: ~7.38); and the outcomes are displayed in Figure 7a-1, b-1 and c-1. As is seen, AIC and MIM molecules are in neutral state at a pH of 7.38; while, MCA transfers to the deprotonated form (d-MCA) in ASW. Thereafter, DFT calculations were carried out on these explicit molecules to acquire global descriptors such as optimized configuration, highest occupied molecular orbital (HOMO), lowest unoccupied molecular orbital (LUMO) and electrostatic potential projection (ESP), which are summarized in Figure 7.

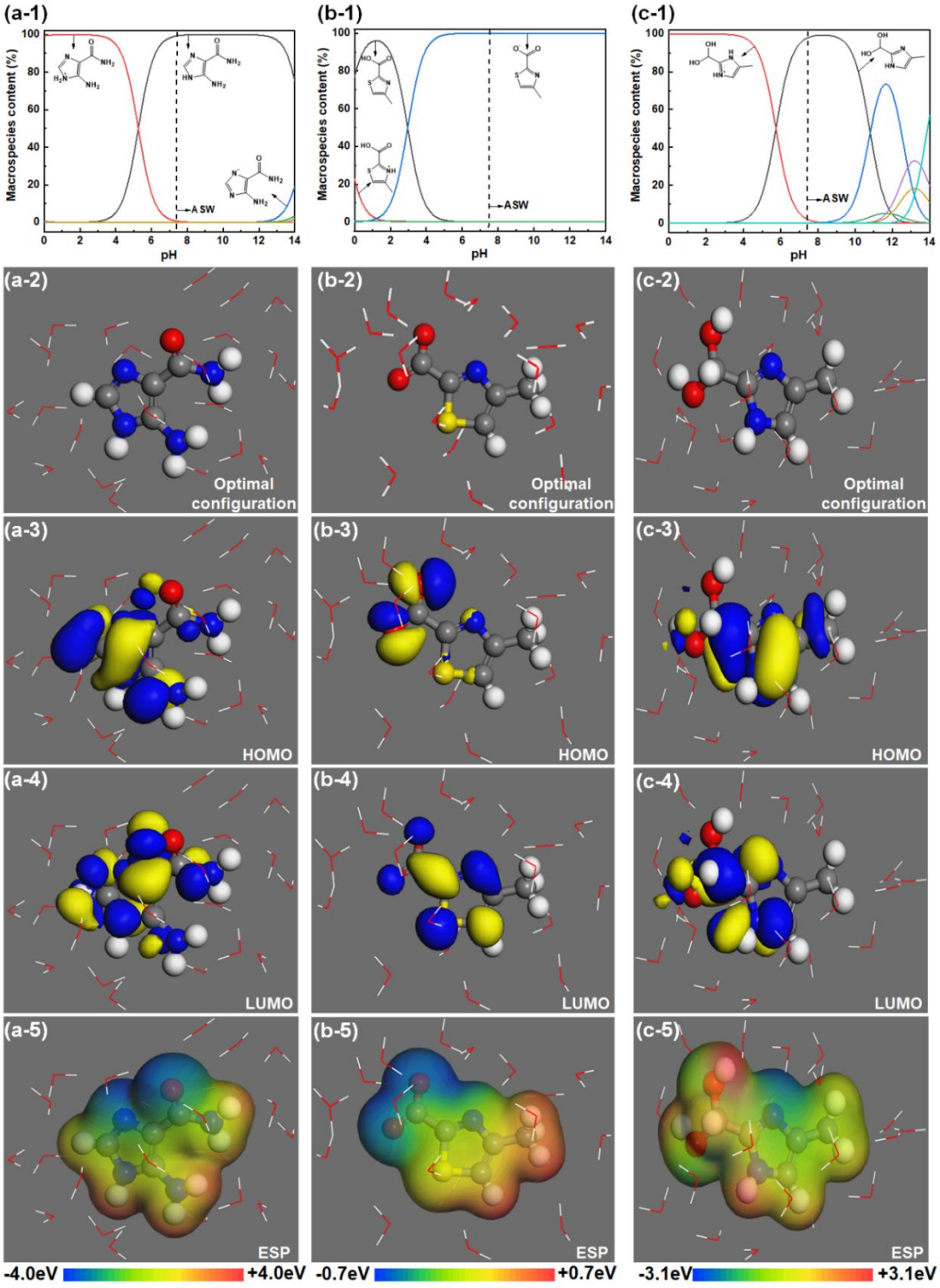

Figure 7. Macro-species analysis (number: 1) and global reactive parameters of AIC (a), d-MCA (b) and MIM (c) in the dominant solvent layer: number 2, optimized configuration; number 3, HOMO distribution; number 4, LUMO distribution; number 5, ESP mapping

According to frontier molecular orbital theory [39], HOMO reflects the reactive sites on an inhibitor to donate surplus electrons, and thus bond with the metal atoms; in turn, LUMO elucidates the capacity of an inhibitor to accommodate electron for the formation of back-donation bond [25, 29]. In

Figure 7a-3 and a-4, AIC possesses the pervasive HOMO and LUMO distributions over the entire molecular backbone, which may facilitate its adsorbing on copper surface via most heteroatoms (i.e. parallel adsorption). ESP mapping of AIC given in Figure 7a-5 indicates that the negative potential primarily concentrates on the amide group. This may be the sensitive center to interact with positively charge copper surface due to oxidation. For d-MCA, HOMO shown in Figure 7b-3 mainly distributes on the deprotonated carboxylic acid moiety; while, LUMO depicted in Figure 7b-4 extends and covers the thiazole ring. Due to the lack of proton, the majority of negative potential on d-MCA (Figure 7b-5) locates on the deprotonated site leaving the other portion with positive potential. In the case of MIM, HOMO spreads over the whole molecular backbone (Figure 7c-3); and LUMO in Figure 7c-4 distributes on the most portion except the methyl terminal. Similar as AIC, the frontier orbital features of MIM may also propel its parallel adsorption on copper surface. In addition, MIM owns the relatively harmonious ESP mapping presented in Figure 7c-5. In comparison with AIC and MIM, d-MCA holds less electrostatic potential encompassing the molecular surface, which tends to adsorb on copper surface through Coulomb attraction rather than charge transfer that requires large electronegativity [7]. Therefore, Coulomb force may be the dominant driving force for depositing d-MCA on the cathodic regions along inner Helmholtz plane at copper/solution interface. The electrostatic adsorption (physisorption) of d-MCA prompts the rapid depletion of pre-accumulated water on copper surface, and subsequently provides a favorable surrounding for the charge transfer between neutral AIC/MIM and copper atoms (i.e. chemisorption). This deeply explains the physicochemical adsorption mechanism of DZPE on copper surface obtained from Langmuir isotherm analysis.

3.4.2 Molecular dynamics simulations

MD simulation is a straightforward way to clarify the adsorption behavior of corrosion inhibitor on metal surface. Figure 8 shows the outcomes of MD simulations for the adsorption of AIC, d-MCA and MIM on Cu (110) plane at 298 K. The stable simulation courses of three adsorption systems are evidenced for the persistent equilibrium of temperature (Figure 8a-1, b-1 and c-1) and energies (Figure 8a-2, b-2 and c-2). Upon the dynamic relaxation, AIC, d-MCA and MIM speedily deposit toward Cu (110) plane, and consequently adopt a near-flat orientation with respect to Cu (110) plane as displayed in Figure 8a-3, b-3 and c-3, respectively. The parallel adsorption originates from the favorable distribution of frontier molecular orbitals as provided by reactive descriptors, which promotes the intensive interaction between inhibitor and the outermost copper atoms. Also, this adsorption configuration is conductive to furthest cover the vulnerable sites, prevent the contact between aggressive species and copper surface, and thus reduce the occurrence probability of corrosion. The favorable adsorption of three compounds on Cu (110) plane can be also characterized by interaction (E_{inter}) and (E_{bind}) energies [17]:

$$E_{inter} = E_{total} - (E_{Cu+Sol} + E_{inh}) = -E_{bind} \quad (14)$$

where E_{total}, E_{Cu+Sol} and E_{inh} are energies of total system, copper substrate with solution and the single inhibitor, respectively. The calculated E_{inter} for AIC, d-MCA and MIM adsorption systems are -113.59, -104.70 and -125.06 kcal/mol, respectively. Negative E_{inter} values reveal the spontaneous

adsorption of each molecular on copper surface, which is in line with the analysis of ΔG_{ads}. Accordingly, relatively large E_{bind} values for all equilibrium processes ascertain the stability of adsorption film for AIC, d-MCA and MIM on Cu (110) plane.

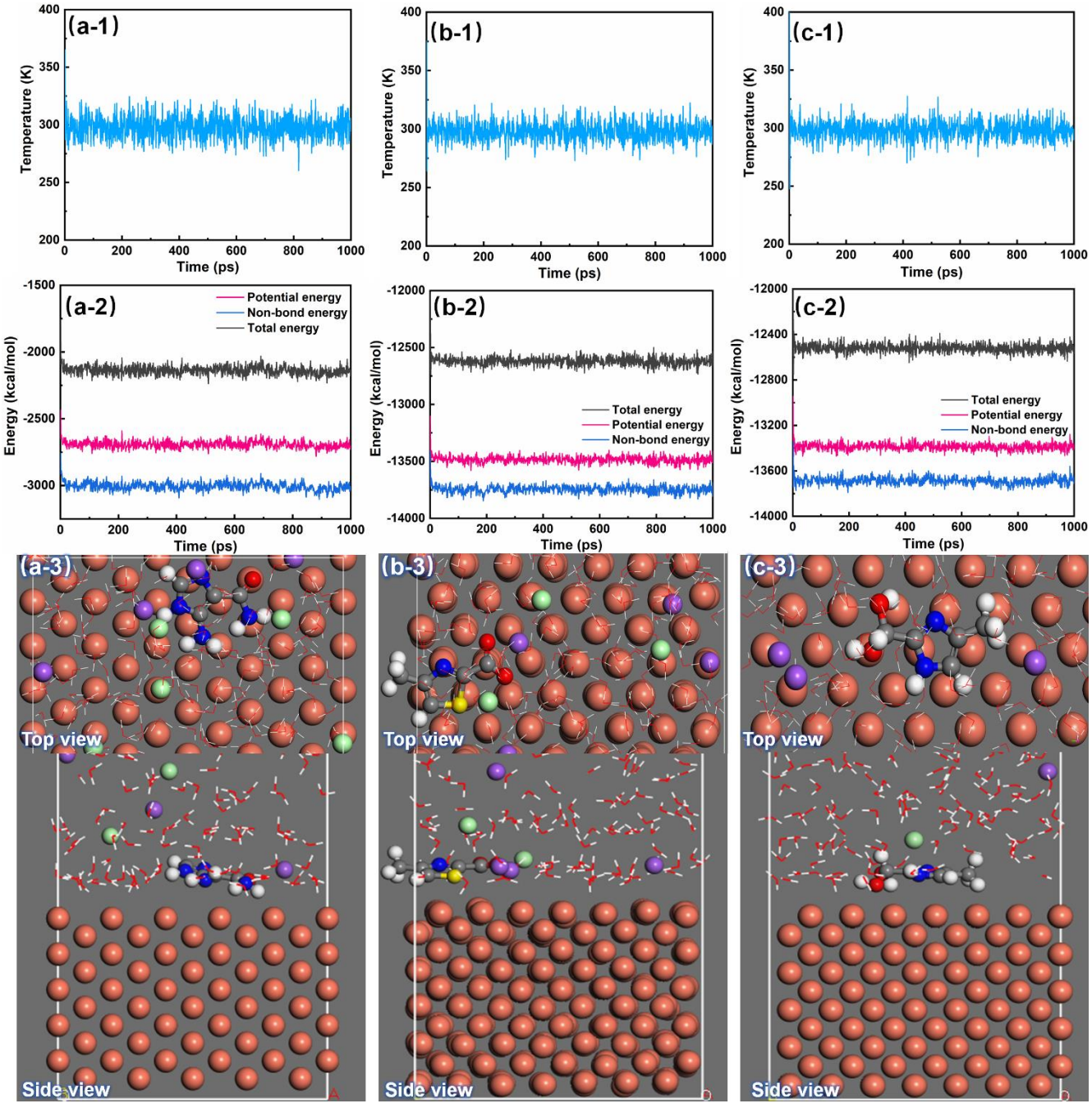

Figure 8. Temperature (upper) and energies (middle) variations for AIC (a), d-MCA (b) and MIM (c) adsorption courses along with their stable configurations on Cu (110) plane (lower)

More authoritative clarification of the interaction between inhibitor and metal surface can be presented by conducting radial distribution functions (RDF) analysis [47]. Figure 9 shows the RDF

outcomes for the interaction between typical heteroatoms on specific compound and copper substrate. Generally, the length (*r*) of initial significant peak emerging less than 3.2 Å reveals the chemical interaction; a value of *r* locating between 3.2 and 5 Å discloses the strong physical interaction; meanwhile, a length larger than 5 Å features the weak van der Waals force [47]. In Figure 9a, the initial peaks for Cu-O and Cu-N interactions lie at 2.79 and 2.91 Å, respectively, which point out the chemical bonding nature of AIC toward copper surface. Because of the protonation effect, the relatively large lengths are observed in Figure 9b for Cu-O (2.86 Å), Cu-S (3.21 Å) and Cu-N (3.03 Å). Thereinto, S atom on d-MCA may be physically linked with copper atom. On the contrary, O and N atoms on d-MCA are still chemically bonded on copper surface. For the adsorption of MIM shown in Figure 9c, Cu-O and Cu-N own the interaction lengths of 2.97 and 2.85 Å, respectively, implying the chemisorption of MIM on Cu (110) plane.

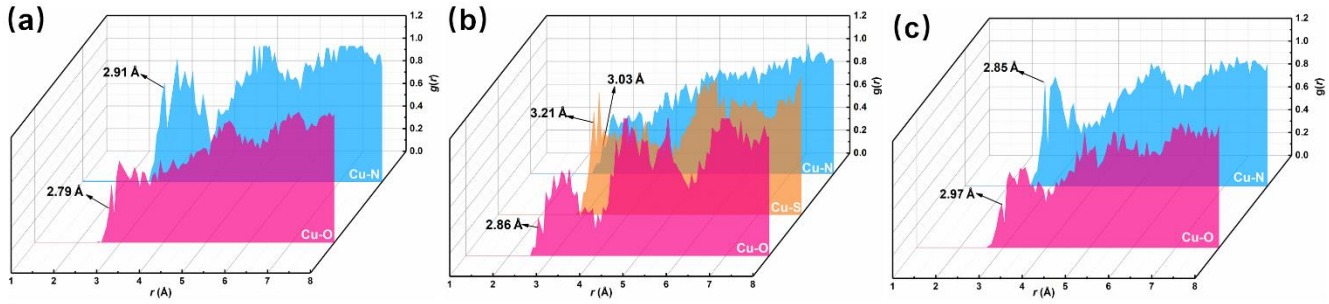

Figure 9. Radial distribution functions for the interaction between heteroatoms on AIC (a), MAC (b) and MIM (c) and surface copper atom

4. CONCLUSIONS

(1) N- and S-contained heterocycle compounds constituted the main species in DZPE, which owned the favorable stability and solubility in the aqueous solution.

(2) Self-consistent electrochemical kinetic analyses from polarization and EFM measurements indicated that DZPE could simultaneously suppress the anodic and cathodic reactions of copper in ASW with a maximum inhibitory efficiency of 95.38% at 298 K. EIS data revealed that the interfacial charge transfer was effectively retarded for copper in the inhibited solution.

(3) The satisfactory anticorrosion effect of DZPE resulted from the efficient adsorption of active components on copper surface, which could be regarded as the mix type inhibitor and obeyed Langmuir isotherm. By virtue of the thorough distributions of frontier molecular orbitals, the neutral state constituents, AIC and MIM, adsorbed on copper surface in a flattened configuration; even if being deprotonated form, d-MCA also followed the parallel adsorption manner.

References

1. D. K. Kozlica, A. Kokalj and I. Milošev, *Corros. Sci.*, 182 (2021) 109082.

2. Y. C. Ma, B. M. Fan, H. Liu, G. F. Fan, H. Hao and B. Yang, *Appl. Surf. Sci.*, 514 (2020) 146086.
3. A. Jmiai, A. Tara, S. El Issami, M. Hilali, O. Jbara and L. Bazzi, *J. Mol. Liq.*, 322 (2021) 114509.
4. G. A. Gaber, S. Hosny and L. Z. Mohamed, *Int. J. Electrochem. Sci.*, 16 (2021) 211214.
5. D. J. Li, X. Q. Zhao, Z. N. Liu, H. Liu, B. M. Fan, B. Yang, X. W. Zheng, W. Z. Li and H. J. Zou, *ACS Omega*, 6 (2021) 29965-29981.
6. B. R. Hou, X. G. Li, X. M. Ma, C. W. Du, D. W. Zhang, M. Zheng, W. C. Xu, D. Z. Lu and F. B. Ma, *npj Mat. Degrad.*, 1 (2017) 4.
7. M. M. Wang, B. M. Fan, B. Y. Wen and C. Jiang, *Sci. China Technol. Sc.*, 63 (2020) 2098–2112.
8. I. B. Obot, A. Meroufel, I. B. Onyeachu, A. Alenazi and A. A. Sorour, *J. Mol. Liq.*, 296 (2019) 111760.
9. N. Chaubey, Savita, A. Qurashi, D. S. Chauhan and M. A. Quraishi, *J. Mol. Liq.*, 321 (2021) 114385.
10. S. H. Alrefaee, K. Y. Rhee, C. Verma, M. A. Quraishi and E. E. Ebenso, *J. Mol. Liq.*, 321 (2021) 114666.
11. R. Samiee, B. Ramezanzadeh, M. Mahdavian, E. Alibakhshi and G. Bahlakeh, *J. Hazard. Mater.*, 398 (2020) 123136.
12. Y. J. Qiang, L. Guo, H. Li and X. J. Lan, *Chem. Eng. J.*, 406 (2021) 126863.
13. L. Guo, R. L. Zhang, B. C. Tan, W. P. Li, H. Y. Liu and S. Z. Wu, *J. Mol. Liq.*, 310 (2020) 113239.
14. S. Z. Salleh, A. H. Yusoff, S. K. Zakaria, M. A. A. Taib, A. Abu Seman, M. N. Masri, M. Mohamad, S. Mamat, S. A. Sobri, A. Ali and P. T. Teo, *J. Clean Prod.*, 304 (2021) 127030.
15. S. G. Meng, Z. N. Liu, X. Q. Zhao, B. M. Fan, H. Liu, M. Guo and H. Hao, *RSC Adv.*, 11 (2021) 31693-31711.
16. H. Movahedinia, M. Shahidi-Zandi and M. Kazemipour, *Int. J. Electrochem. Sci.*, 16 (2021) 210228.
17. A. Farhadian, A. Rahimi, N. Safaei, A. Shaabani, E. Sadeh, M. Abdouss and A. Alavi, *ACS Appl. Mater. Inter.*, 13 (2021) 3119-3138.
18. X. Zhang, W. P. Li, G. C. Yu, X. L. Zuo, W. Luo, J. Zhang, B. C. Tan, A. Q. Fu and S. T. Zhang, *J. Mol. Liq.*, 318 (2020) 114080.
19. I. B. Obot, D. D. Macdonald and Z. M. Gasem, *Corros. Sci.*, 99 (2015) 1-30.
20. C. Verma, H. Lgaz, D. K. Verma, E. E. Ebenso, I. Bahadur and M. A. Quraishi, *J. Mol. Liq.*, 260 (2018) 99-120.
21. W.-Y. J. Kam, F. Abas, N. Hussain and H. Mirhosseini, *Nat. Prod. Res.*, 34 (2020) 13.
22. B. M. Fan, G. Wei, H. Hao, A. R. Guo and J. Li, *Desalin. Water Treat.*, 57 (2016) 17308-17321.
23. H. M. Jiang, J. Dong, S. J. Jiang, Q. X. Liang, Y. Zhang, Z. H. Liu, C. Y. Ma, J. M. Wang and W. Y. Kang, *Food Res. Int.*, 136 (2020) 109316.
24. R. Natarajan and F. S. Zahir Said Al Shibli, *Chemosphere*, 284 (2021) 131375.
25. A. Singh, K. R. Ansari, M. A. Quraishi and S. Kaya, *J Mol. Struct.*, 1206 (2020) 127685.
26. D. S. Chauhan, K. E. Mouaden, M. A. Quraishi and L. Bazzi, *Int. J. Biol. Macromol.*, 152 (2020) 234-241.
27. H. Liu, B. M. Fan, G. F. Fan, X. Q. Zhao, Z. N. Liu, H. Hao and B. Yang, *J. Alloy. Compd.*, 872 (2021) 159752.
28. N. Rajamohan, F. S. Z. S. Al Shibli and M. Rajasimman, *Environ. Res.*, 203 (2021) 111816.
29. H. Lgaz, S. K. Saha, A. Chaouiki, K. S. Bhat, R. Salghi, Shubhalaxmi, P. Banerjee, I. H. Ali, M. I. Khan and I.-M. Chung, *Constr. Build. Mater.*, 233 (2020) 117320.
30. H. Liu, B. M. Fan, G. F. Fan, Y. C. Ma, H. Hao and W. Zhang, *J. Mater. Sci. Technol.*, 72 (2021) 202-216.
31. B. M. Fan, Y. C. Ma, M. M. Wang, H. Hao, B. Yang, J. Y. Lv and H. Sun, *J. Mol. Liq.*, 292 (2019) 111446.
32. A. Saady, Z. Rais, F. Benhiba, R. Salim, K. Ismaily Alaoui, N. Arrousse, F. Elhajjaji, M. Taleb, K. Jarmoni, Y. Kandri Rodi, I. Warad and A. Zarrouk, *Corros. Sci.*, 189 (2021) 109621.

33. Y. C. Ma, B. M. Fan, H. Hao, J. Y. Lu, Y. H. Feng and B. Yang, *Chem. J. Chinese U.*, 40 (2019) 96-107.
34. B. M. Fan, Z. N. Liu, X. Q. Zhao, H. Liu, G. F. Fan and H. Hao, *Colloid. Surface. A*, 629 (2021) 127434.
35. I. B. Obot and I. B. Onyeachu, *J. Mol. Liq.*, 249 (2018) 83-96.
36. Y. Zhou, P. Zhang, L. H. Z. Su, B. M. Fan and F. Yan, *Mater. Lett.*, 304 (2021) 130640.
37. H. M. Elaryian, M. A. Bedair, A. H. Bedair, R. M. Aboushahba and A. E.-A. S. Fouda, *J. Mol. Liq.*, 346 (2022) 118310.
38. H. Liu, B. M. Fan, Z. N. Liu, X. Q. Zhao, B. Yang, X. W. Zheng and H. Hao, *J. Ind. Eng. Chem.*, (2021) https://doi.org/10.1016/j.jiec.2021.11.004.
39. Y. C. Ma, T. T. Zhou, W. Q. Zhu, B. M. Fan, H. Liu, G. F. Fan, H. Hao, H. Sun and B. Yang, *J. Mol. Model.*, 26 (2020) 81.
40. L. Guo, J. H. Tan, S. Kaya, S. L. Leng, Q. B. Li and F. Zhang, *J. Colloid Interf. Sci.*, 570 (2020) 116-124.
41. Y. C. Ma, B. M. Fan, M. M. Wang, B. Yang, H. Hao, H. Sun and H. J. Zhang, *Chem. J. Chinese U.*, 40 (2019) 1706-1716.
42. K. R. Ansari, D. S. Chauhan, M. A. Quraishi, M. A. J. Mazumder and A. Singh, *Int. J. Biol. Macromol.*, 144 (2020) 305-315.
43. Y. C. Ma, B. M. Fan, T. T. Zhou, H. Hao, B. Yang and H. Sun, *Polymers*, 11 (2019) 635.
44. B. M. Fan, H. Hao, B. Yang and Y. Li, *Res. Chem. Intermediat.*, 44 (2018) 5711-5736.
45. A. H. Tantawy, K. A. Soliman and H. M. Abd El-Lateef, *J. Clean. Prod.*, 250 (2020) 119510.
46. B. M. Fan, H. Hao, A. R. Guo and R. P. Yang, *J. Water Reuse Desal.*, 6 (2016) 399-412.
47. G. F. Fan, H. Liu, B. M. Fan, Y. C. Ma, H. Hao and B. Yang, *J. Mol. Liq.*, 311 (2020) 113302.